Original Research Article

Numerical simulation study of dredger impeller based on fluid-solid coupling

ABSTRACT

Aims: The majority of current research on submerged impellers concentrates on transient hydrodynamic properties; however, the modifications to the flow field and impeller caused by fluid-solid interaction have not been sufficiently studied.
Study design: The vibration and deformation of the impeller due to the flow field's changing flow velocity will have an impact on the impeller's stability.
Methodology: In this study, two-way fluid-structure coupling is used to investigate variations in impeller dynamic stress as well as changes in the flow field's properties at various inlet velocities.
Results: The larger the flow velocity, the smaller the impeller's final deformation is, and the difference between the deformation at various flow velocities is approximately. 2%. The analysis and comparison of the maximum equivalent force diagrams at various velocities reveals that the maximum equivalent force in the impeller increases from 4.0615 MPa to 62.323 MPa with an increase in the flow velocity, exhibiting a jump growth. the maximum stress occurs at the beginning of the impeller's movement and reaches a maximum of 173.17 MPa. The maximum stress decreases with increasing flow field inlet velocity, falling to 168.65 MPa and 159.37 MPa at 2m/s and 3m/s, respectively.

Conclusion: The results based on the two-phase flow model and k-turbulence model demonstrate that the impeller deformation increases stepwise from inside to outside, and the total deformation of the impeller decreases as the flow field's inlet velocity increases. The maximum stress of the impeller first appears at the junction of the hub and the fan blade, where the stress decreases with the increase of flow velocity, and the maximum stress appears in the middle of the impeller.

Keywords: Impeller blades; bi-directional fluid-solid coupling; dynamic stress distribution; deformation; flow field analysis

1. INTRODUCTION

The impeller, which is the most significant component of the dredger's mixing system, must supply the necessary force and favorable flow conditions throughout the task, and the fluid must adhere to its structural specifications in order for mass transfer to be strengthened and efficient mixing to occur. The study and simulation of the impeller can serve as a crucial foundation for the construction of the dredger because the impeller must operate under challenging situations, such as varied flow velocity, varying muck concentrations, and a variety of contaminants in the water. It has been demonstrated that there is a force coupling effect between the relative motion of the impeller and the fluid, and as a result, the impeller will deform throughout the motion, and the flow field structure is affected by the impeller deformation, which changes the distribution and strength of fluid forces, which modifies the properties of fluid transfer and mixing.[1] Many academics have studied the characteristics of impellers in light of the advancement of simulation technology. Gu et al. used the CFD simulation technique to examine the fluid dynamics of the fractal impeller in the solid-liquid mixing process. The solid-particle suspension quality of the fractal impeller was found to be better under the same power consumption than that of the four-slant impeller, and the suspension quality of the fractal impeller increased as the number of fractal impeller fractal iterations increased[2] . Eight high-speed rotating impellers were tested for mixing effectiveness in the agitated charge's turbulent condition by Fort and others. The testing outcomes demonstrated that, in comparison to conventional impellers with inclined blades, axial impellers with fractal blades can maximum energy savings[3] . Devi et al. investigated the mass transfer coefficients and power consumption capabilities of a double impeller alone and a double

impeller combined with a curved impeller simultaneously using computational fluid dynamics. It was discovered that the bent impeller had a higher power consumption capacity in both the single- and double-impeller scenarios[4] . The fluid dynamics of gas-liquid dispersion in rigid impeller and rigid-flexible impeller stirring were studied by Liu et al. using a combination of computational fluid dynamics (CFD) and population equilibrium model (PBM). The findings revealed that the longer length of the flexible connecting piece facilitated the gas-liquid dispersion process and that the ideal pore ratio and pore size for the gas-liquid dispersion process were, respectively, 12% and 8 mm[5] . However, Li et al.'s study of the hydrodynamic properties of a hollow self-induced impeller in the mixing process revealed that, in the case of inflation, the impeller power was affected by the flow rate, and that, by using a CFD simulation, the power consumption decreased as the impeller clearance increased while the flow rate increased at the same impeller speed[6] . By using coupled calculations, Liang et al. were able to simulate the interaction of the fluid with the impeller and turbine fixed on a flexible shaft during the mixing process. They then examined in detail the different loads placed on the impeller based on experimentally validating the simulated impeller torque and dimensionless shaft bending moment. The results revealed that the shaft bending moment was primarily brought on by the lateral force placed on the impeller and the impeller mass imbalance[7] . On the other hand, Qian et al. investigated the impeller's vibration when it was submerged. After optimizing the impeller, it was discovered that there was an unequal distribution of energy due to a relative velocity gradient between the suction and pressure sides of the impeller. By maximizing the impeller thickness, the vibration performance of the impeller was improved[8] . In this paper, the numerical simulation of the impeller and its flow field is mainly carried out by the bi-directional fluid-solid coupling method to study the effect of flow velocity on the impeller stress variation and the flow field characteristics.

2. FLUID-SOLID COUPLING CALCULATION

2.1 Physical model and calculation method

To construct a condensed experimental model, the model in this article is based on the dimensional structure of the real dredger impeller. Figure 1 displays the exact 3D model. The fluid domain is a drum-shaped area that entirely encloses the impeller and the rotor shaft, including an inlet and an outlet, and the impeller has three blades. The impeller speed is 300 r/min

Bidirectional fluid-structure coupling is used because the impeller is located in the fluid domain during the numerical simulation process and forces acting on it and the fluid are equal and opposite. Since both the fluid domain and the structural domain have forces acting upon them, the two-way fluid-structure coupling method solves the solid structure of the model and the fluid domain separately before exchanging the data in both directions. As a result, the method can calculate the structural deformation of the solid structure under the force of the fluid, the maximum stress, among other things, though it takes longer to calculate[9]

According to the fluid-solid coupling calculation concept, each time a transient calculation is run, the fluid domain is initially solved in each of the many time steps that make up the total calculation time. Second, the solid domain is solved using the ANSYS solver in the order of strain and stress in accordance with the solid domain mesh division and imposed constraints. This allows the fluid domain mesh to be deformed in accordance with the magnitude of the structural deformation displacement calculated in the solid domain and fed back to the fluid domain to determine the impact of the solid domain deformation on the flow field. The outcomes of this time step will then be utilized as the starting point for the following time step, and so on. It is clear from the two-way fluid-solid coupling calculation method that each time step needs to be linked multiple times since data flow between the fluid domain and the solid domain is two-way.

Due to the short amount of time required for the impeller rotation to reach steady state, a time step of 0.5 seconds is used in this calculation, and a total of 100 steps are calculated.

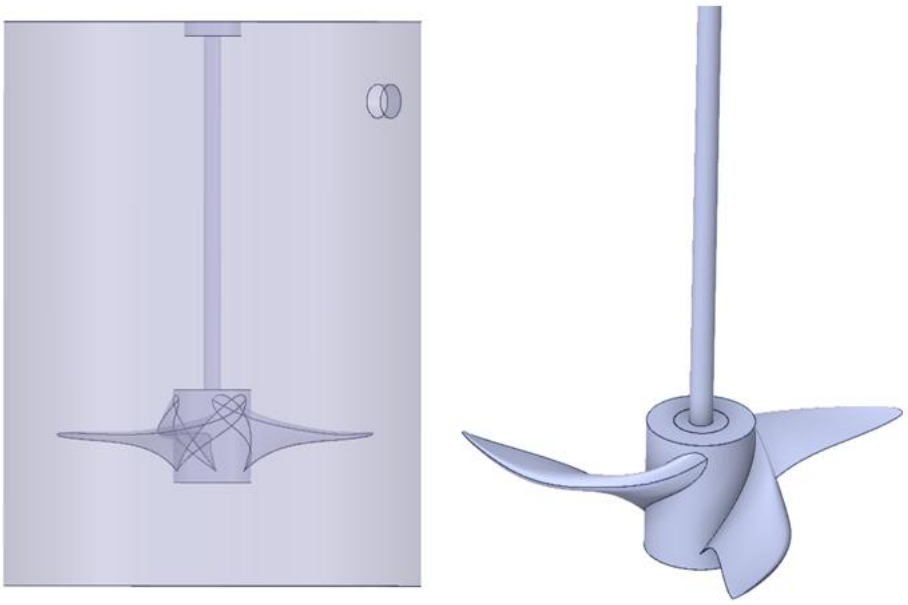

Fig. 1. Physical model.

2.2 Two-phase flow model

A mud-water combination serves **as** the internal flow field for this computation, and the flow of the mud is represented by a conventional multiphase flow model[10]. Additionally, the main phase, magnitude, and direction of its motion are essentially the same. As a result, it may be claimed that this experiment uses the mixed two-phase flow model. And the following conditions are met for the mixture's continuity equation:

$$\frac{\partial}{\partial t}(\rho_m) + \nabla \cdot (\rho_m \vec{v}_m) = 0 \quad (1)$$

$$\vec{v}_m = \frac{\Sigma_{k=1}^{n} \alpha_K \rho_k \vec{v}_k}{\rho_m} \quad (2)$$

$$\rho_m = \sum_{k=1}^{n} \alpha_1 \rho_k \quad (3)$$

2.3Turbulence model

The turbulence model uses$k-\varepsilon$ turbulence equations with water as the sealing medium, temperature is considered as a constant value, and the pressure, density and momentum terms use a second-order discretization scheme. The turbulent kinetic energy and turbulent dissipation rate terms are used in a first-order scheme[11] , which has a good convergence rate and relatively low memory requirements, and is really good for solving external flow problems around complex geometries. For incompressible fluids, the general expression is

$$\rho \frac{\partial u_i}{\partial t} + u_j \rho \frac{\partial u_i}{\partial x_j} = -\frac{\partial P}{\sigma x_i} + \mu \frac{\partial^2 u_i}{\partial x_j^2} + \rho f_i \quad (4)$$

$$\frac{\partial(\rho k)}{\partial t} + \frac{\partial(\rho k u_i)}{\partial x_i} = \frac{\partial}{\partial x_i}\left(\alpha_i \mu \frac{\partial k}{\partial x_i}\right) G_k + \rho_\varepsilon \quad (5)$$

$$\frac{\partial(\rho \varepsilon)}{\partial t} + \frac{\partial(\rho \varepsilon u_i)}{\partial x_i} = \frac{\partial}{\partial x_i}\left(\alpha_\varepsilon \mu \frac{\partial \varepsilon}{\partial x_j}\right) + \frac{C_{1\varepsilon}}{k} G_k - C_{2\varepsilon} \rho \frac{\varepsilon^2}{k} \quad (6)$$

Where i ,j = 1, 2, 3;$\rho \frac{\partial u_i}{\partial t}$ is the non-constant term;$u_j \frac{\partial u_i}{\partial x_j}$ is the convective term;$\mu \frac{\partial^2 u_i}{\partial x_j^2}$ is the diffusion term;ρf_i is the volume force;$C_{1\varepsilon}$ =1.42;$C_{2\varepsilon}$ =1.68;ε is the dissipation rate.

Where $\vec{v}_m$ is the mass-averaged velocity;ρ_m is the density of the mixture;α_K is the volume fraction of phase K.

2.4 Mesh division

The impeller of the dredger is made of aluminum alloy and the rotor is made of structural steel; the specific parameters are as follows Table 1

Table 1. Material Property Parameters.

	Material	density	Yield strength	Coefficient of elasticity	Bending strength
impeller	Aluminum alloy	$2700kg{\cdot}m^{-3}$	55.2 MPa	$6.89\times10^{10}Pa$	103MPa
Rotating shaft	Structural steel	$7.85\times10^{3}kg{\cdot}m^{-3}$	235MPa	$2.06\times10^{11}Pa$	415MPa

In order to account for the impeller's small tip gap in relation to its size, the number of effective nodes, and a smooth transition of the tip gap mesh from the internal mesh of the impeller, Figures 2 and 3 show the meshes of the solid structure and the fluid domain, respectively. Tetrahedral mesh is used to create the fluid domain's mesh. Figure 2 contains 1346310 fluid domain meshes in total, with the type of mesh cell being Solid186. The hybrid mode can be used to calculate the almost incompressible elastic-plastic material and the completely incompressible hyperplastic material in order to analyze its maximum stress as well as maximum deformation. The cell consists of 20 nodes, and each node has three degrees of freedom in different directions, meaning it has arbitrary spatial characteristics.

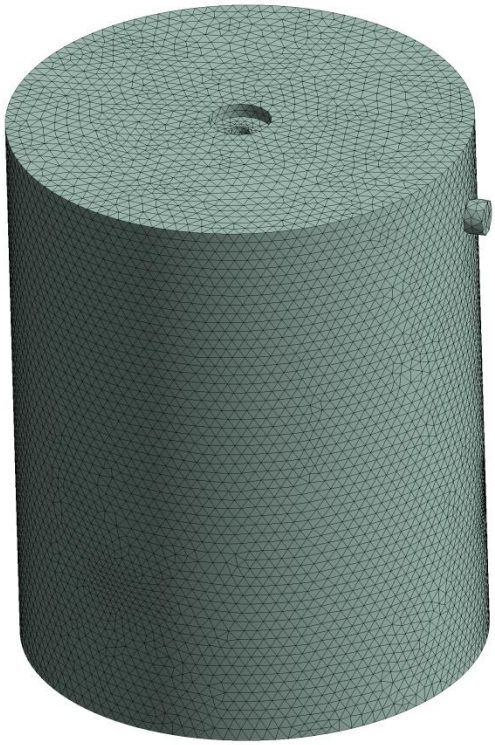

Fig.2. Fluid domain grid.

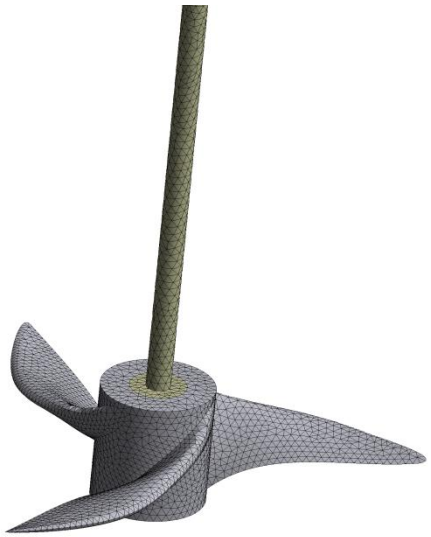

Fig.3. Solid grid.

Figure 4 shows the maximum equivalent force of the impeller surface in the fluid domain at different numbers of grid cellsF_{Emax} The variation curves of the impeller surface at different numbers of grid cells in the fluid domain are shown in Figure 4, and the corresponding numbers of grids in the fluid domain are 501324, 1017832, 1346310, 1786438, 2246579, etc. The analysis in Figure 4 shows that when the number of grids is greater than 1000000, theF_{Emax} This indicates that the increase in the number of grids has little effect on the results of the final simulation, and the calculation error is within ±5%, which meets the requirements of the grid independence test.

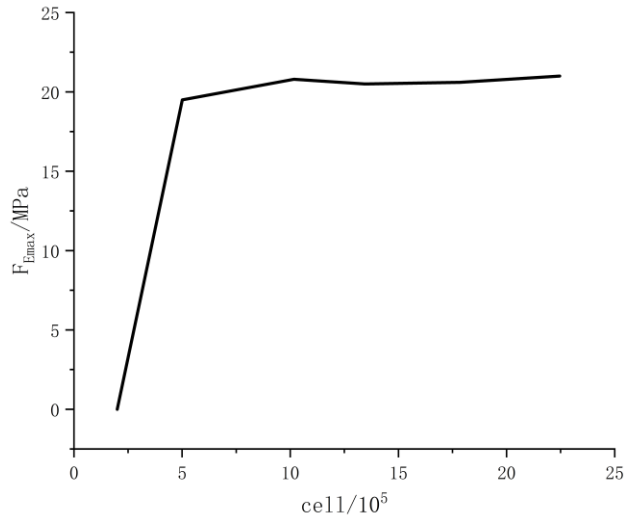

Fig.4. Different grid cells ofF_{Emax} variation.

2.5 Boundary conditions

The boundary conditions for the two-way fluid-solid coupling are also split into the fluid domain and solid domain. In the fluid domain, gravity acceleration, inlet velocity, and outlet pressure can all be adjusted. Set the connection between the rotating shaft and the ground for the solid domain in order to add the impeller's rotational speed; add a fixed support to the bearing to prevent the solid structure's radial displacement; add a rotating connection between the bearing and the rotating shaft to ensure the impeller rotates freely relative to the bearing; and add the gravitational acceleration in the opposite direction of the Y-axis to t.; impeller added As illustrated in Figure 5, the impeller surface is added as the flow-solid intersection surface so that information can be exchanged with the flow field in both directions during the coupling calculation.

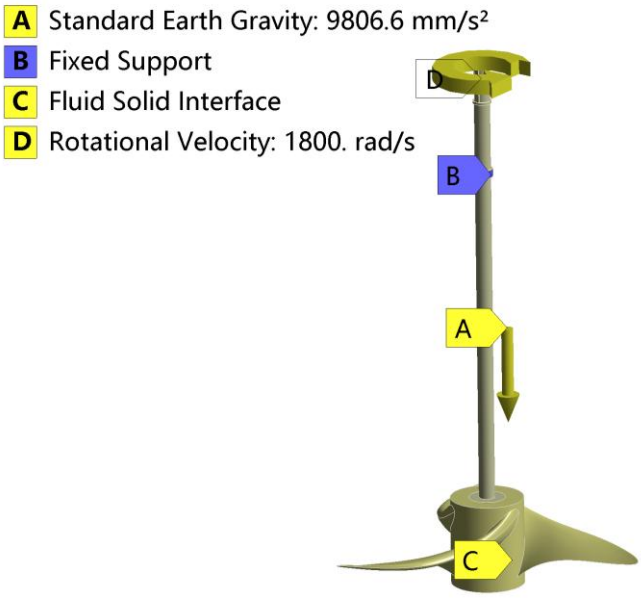

Fig.5. Schematic diagram of impeller load constraint.

3. CALCULATION RESULTS AND DISCUSSION

The force deformation and maximum stress of the impeller under various conditions of the inlet velocity of 1m/s, 2m/s, and 3m/s in the fluid domain were separately calculated[12,13] in order to analyze the total deformation and maximum stress of the impeller under the action of the flow field more thoroughly.

3.1 Total impeller deformation

Figure 6 depicts the impeller model's deformation at a specific time with inlet velocities of 1 m/s, 2 m/s, and 3 m/s in the fluid domain, respectively. The impeller deformation is shown in the figure to be stepped from the impeller root to the impeller tip; the minimum deformation is shown at the impeller root and the maximum deformation is shown at the impeller tip, indicating that the impeller deformation increases gradually as the linear velocity increases. The inlet of the flow field has less of an impact on the maximum deformation of the impeller. The maximum deformation of the impeller and the inlet velocity of the flow field are negatively associated, and the maximum deformation of the impeller decreases as the flow velocity increases. Therefore, the inlet velocity of the flow field can be increased appropriately under the assumption that it will meet the actual production needs.

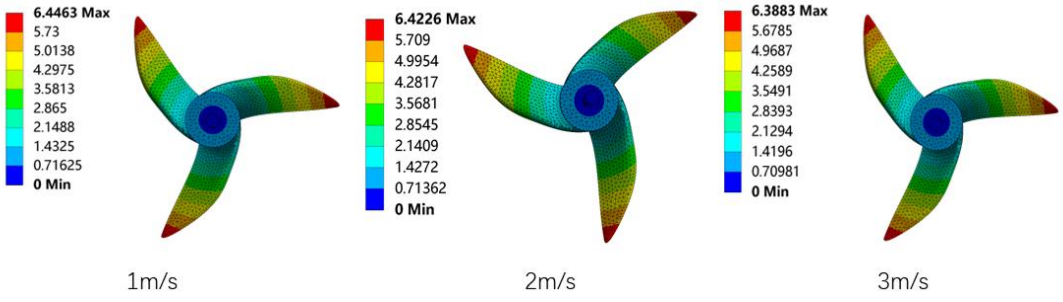

Fig.6. Total impeller deformation.

The curve of the impeller's maximum deformation over time under a flow field with various inlet velocities is shown in Figure 7. The illustration shows that the impeller's maximum deformation is linearly proportional to time, that it grows over time, and that it eventually stabilizes. The flow field velocity is essentially unaffected by the maximum deformation of the impeller during the first 80-time steps, after which the maximum deformation of the impeller stabilizes. The larger the flow velocity, the smaller the impeller's final deformation is, and the difference between the deformation at various flow velocities is approximately. 2%.

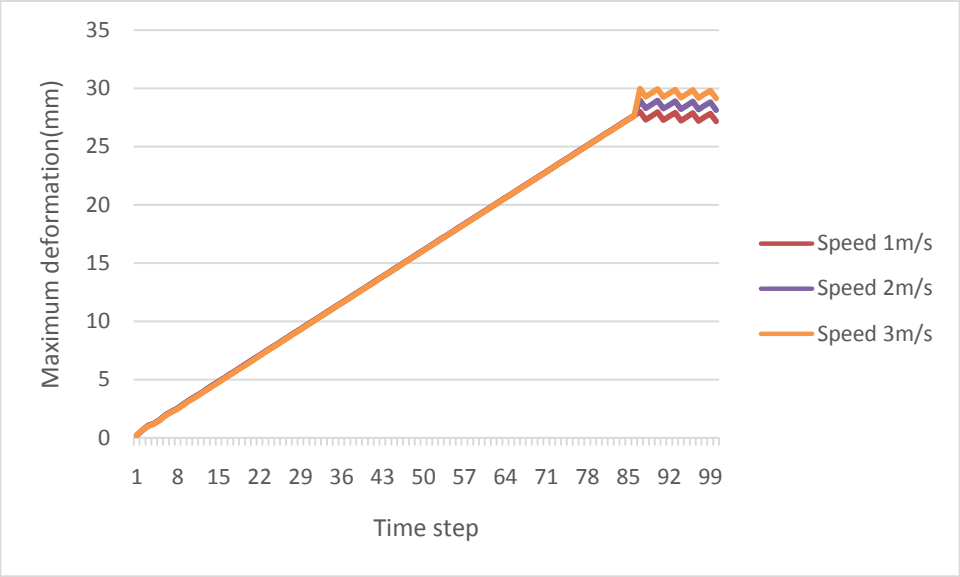

Fig.7. impeller deformation curve.

3.2 Maximum impeller stress

Figure 8 depicts the maximum equivalent force of the impeller with simultaneous changes in the inlet velocities of the flow field. The maximal equivalent force of the impeller is spread in the position of the fan blade of the impeller against the top, and its range is elliptical, as can be seen in the image. As the range widens, the stress gradually decreases from the inside to the outside. The analysis and comparison of the maximum equivalent force diagrams at various velocities reveals that the maximum equivalent force in the impeller increases from 4.0615 MPa to 62.323 MPa with an increase in the flow velocity, exhibiting a jump growth. This indicates that the flow field inlet velocity has a greater influence on the maximum equivalent force in the impeller than previously thought. The maximum stress increases as the flow velocity increases. The greatest stress point is a hazardous area vulnerable to structural failure [14,15]. As a result, it demands attention.

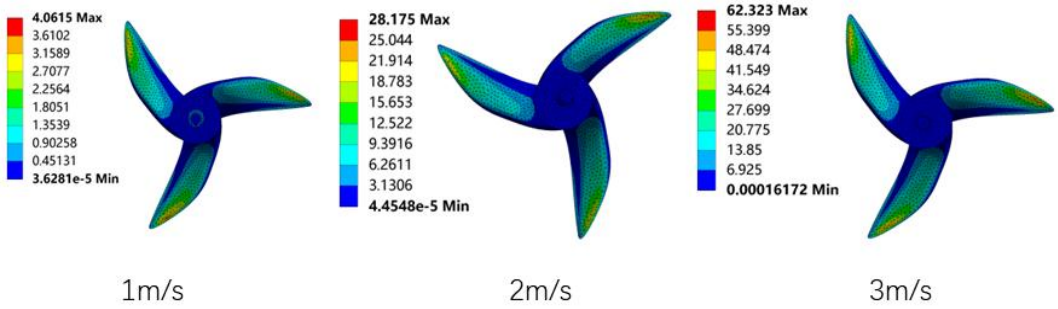

Fig.8. Maximum impeller stress.

As depicted in Figure 9, the maximum stress occurs at the beginning of the impeller's movement and reaches a maximum of 173.17 MPa. The maximum stress decreases with increasing flow field inlet velocity, falling to 168.65 MPa and 159.37 MPa at 2m/s and 3m/s, respectively. The impeller's remaining components are currently under very little stress. Combining Figures 10 and 11, we can see that the stress at the impeller's root is highest at first, then it decreases sharply as it rotates and tends to stabilize after about 10-time steps. The stress distribution of the impeller following stabilization is examined in the above figure. In order to improve the impeller stability, it is necessary to treat the fan blade or impeller root differently when facing different inlet velocities. The greater the flow field velocity, for example, the smaller the stress on the impeller root, but the greater the maximum stress on the fan blade when the impeller is rotating smoothly.

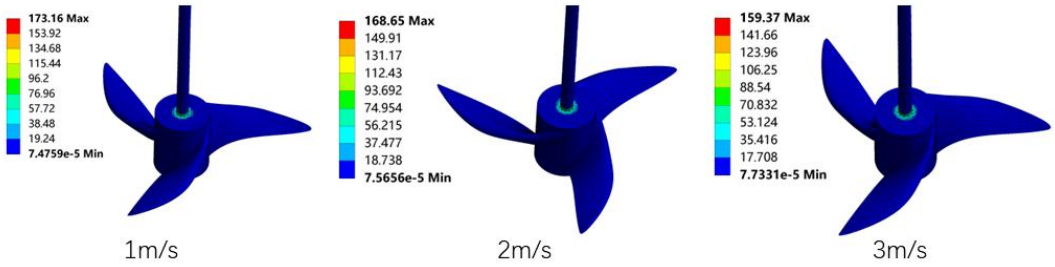

Fig.9. Maximum stress at the initial moment.

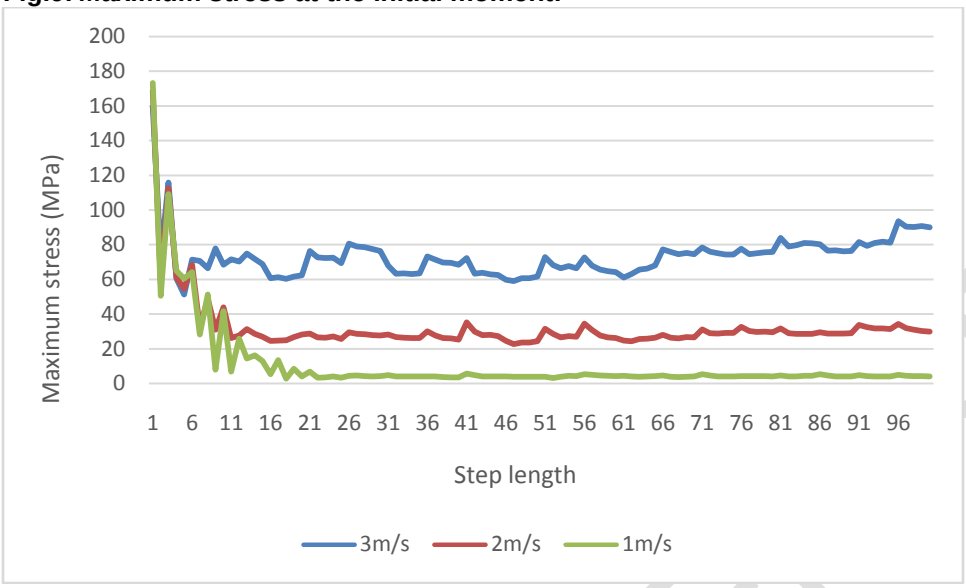

Fig.10. Maximum stress curve.

4. CONCLUSION

The dynamic stress of the dredger impeller in the two-phase flow field was calculated using the two-way fluid-solid coupling method, and the results were used to determine the following: the relationship between the flow field's inlet velocity and the total stress and deformation of the impeller, the change law of the velocity and pressure of the impeller flow field, and the areas of the impeller where wear may occur.

(1) The maximum deformation of the impeller grows and grows as the time step increases, eventually tending to a stable value. When the inlet velocity of the flow field increases, the total deformation of the impeller decreases. The impeller's deformation is stepped from the root to the top and is evenly distributed. The more outward the deformation, the larger it is.

(2) The location of the fan blade against the top of the impeller is where the highest equivalent stress of the impeller is distributed; the flow field entrance velocity has a stronger impact on the impeller's stress, and the higher the flow velocity, the higher the maximum stress; The intersection of the fan blade and the hub is where the impeller's maximum stress first appears during rotation. The maximum stress and inlet velocity are inversely correlated, with the maximum stress decreasing as the inlet velocity increases and the stress on the impeller's root decreasing as the flow field velocity increases. The maximum stress on the fan blade when the impeller is rotating smoothly increases as the field flow rate increases, but the tension on the impeller root decreases. In order to prevent stress concentration, the impeller should actually be thickened at various points in accordance with various flow field velocities.

ETHICAL APPROVAL (WHERE EVER APPLICABLE)

"All authors hereby declare that all experiments have been examined and approved by the appropriate ethics committee and have therefore been performed in accordance with the ethical standards laid down in the 1964 Declaration of Helsinki."

REFERENCES

1. Zhu Jun; Zhou Zhenglin; Liu Zuohua; Zheng Xiongpan; Liu Renlong; Tao Changyuan; Wang Yundong. Fluid-solid coupling behavior of rigid-flexible combined stirring paddles for enhanced fluid mixing. Journal of Chemical Engineering 2015, 66, 3849-3856.

2. Gu, D.; Cheng, C.; Liu, Z.; Wang, Y. Numerical simulation of solid-liquid mixing characteristics in a stirred tank with fractal impellers. Advanced Powder Technology 2019, 30, 2126-2138, doi: 10.1016/j.apt.2019.06.028.

3. Fort, I.; Seichter, P.; Pesl, L.; Rieger, F.; Jirout, T. BLENDING CHARACTERISTICS OF HIGH-SPEED ROTARY IMPELLERS. Chemical and Process Engineering-Inzynieria Chemiczna I Procesowa 2013, 34, 427-434, doi:10.2478/cpe-2013-0035.

4. Devi, T.T.; Kumar, B. Mass transfer and power characteristics of stirred tank with Rushton and curved blade impeller. Engineering Science and Technology-an International Journal-Jestech 2017, 20, 730-737, doi:10.1016/j.jestch.2016.11.005.

5. Gu, D.Y.; Liu, Z.H.; Tao, C.Y.; Li, J.; Wang, Y.D. Numerical Simulation of Gas-Liquid Dispersion in A Stirred Tank Agitated by Punched Rigid-Flexible Impeller. International Journal of Chemical Reactor Engineering 2019, 17, doi:10.1515/ijcre-2018-0196.

6. Li, L.C.; Chen, N.; Xiang, K.F.; Xiang, B.P. CFD simulation of hydrodynamics characteristics in a tank stirred by a hollow self-inducing impeller. Canadian Journal of Chemical Engineering 2018, 96, 1837-1848, doi:10.1002/cjce.23135.

7. Liang, Y.Y.; Gao, Z.M.; Shi, D.E.; Zhao, W.L.; Cai, Z.Q. Coupling simulation of fluid structure interaction in the stirred vessel with a pitched blade turbine. Chinese Journal of Chemical Engineering 2018, 26, 922-929, doi:10.1016/j.cjche.2017.10.026.

8. Qian, B.; Wu, P.; Huang, B.; Zhang, K.; Li, S.Y.; Wu, D.Z. Optimization of a Centrifugal Impeller on Blade Thickness Distribution to Reduce Hydro-Induced Vibration. Journal of Fluids Engineering-Transactions of the Asme 2020, 142, doi:10.1115/1.4044965.

9. Li, W.; Ji, L.L.; Shi, W.D.; Zhou, L.; Jiang, X.P.; Zhang, Y. Vibration characteristics of the impeller at multi-conditions in mixed-flow pump under the action of fluid-structure interaction. Journal of Vibroengineering 2016, 18, 3213-3224, doi:10.21595/jve.2016.16776.

10. Zhang, M.; Wang, X.F.; Xu, S.L.; Wang, W. Numerical Simulation of the Flow Field in Circumferential Grooved Liquid Seals. Advances in Mechanical Engineering 2013, doi:10.1155/2013/797201.

11. Rajappan, R.; Mahalakshmi, N.V. Computational study of free-stream turbulence effects on film cooling using two different models. Progress in Computational Fluid Dynamics 2011, 11, 96-104, doi:10.1504/pcfd.2011.038835.

12. Li, W.; Ji, L.; Shi, W.; Zhou, L.; Jiang, X.; Zhang, Y. Fluid-structure interaction study of a mixed-flow pump impeller during startup. Engineering Computations 2018, 35, 18-34, doi:10.1108/ec-01-2016-0043.

13. Kan, K.; Zheng, Y.; Fu, S.; Liu, H.; Yang, C.; Zhang, X. Dynamic stress of impeller blade of shaft extension tubular pump device based on bidirectional fluid-structure interaction. Journal of Mechanical Science and Technology 2017, 31, 1561-1568, doi:10.1007/s12206-017-0303-1.

14. Liu, X.; Xu, F.; Cheng, L.; Pan, W.; Jiao, W. Stress Characteristics Analysis of Vertical Bi-Directional Flow Channel Axial Pump Blades Based on Fluid-Structure Coupling. Machines 2022, 10, doi:10.3390/machines10050368.

15. Huang, C.; Liu, Z.; Liu, Z.; Hao, C.; Li, D.; Luo, K. Motion Characteristics of High-Speed Supercavitating Projectiles Including Structural Deformation. Energies 2022, 15, doi:10.3390/en15051933.

16. Jeong, Jungjun; Oh, Sanghan; Son, C.-H. Numerical Analysis of the Flow Field of Circular Nozzle Exit Region. The KSFM Journal of Fluid Machinery 2010, 13, 13-18.

17. Guo, Y.L.; Yang, C.X.; Wang, Y.; Lv, T.Z.; Zhao, S. Study on Inlet Flow Field Structure and End-Wall Effect of Axial Flow Pump Impeller under Design Condition. Energies 2022, 15, doi:10.3390/en15144969.

18. Han-Yong Jeon; Jung-Jae Ryu; Dae-Young Heo. Evaluation of Abrasion Resistance of Geosynthetics by Rotational Abrasion Test. Textile Science and Engineering 2004, 41, 133-139.

19. Liu, X.; Kan, F.; Wang, H.; Xin, X.; Wang, Z.; Huang, H. Fatigue life prediction of clutch sleeve based on abrasion mathematical model in service period. Fatigue & Fracture of Engineering Materials & Structures 2020, 43, 488-501, doi:10.1111/ffe.13133.